Editors' Suggestion | Featured in Physics

Stochastic Elastohydrodynamics of Soft Valves

Mengfei He,[1] Sungkyu Cho,[2] Gianna Dafflisio,[2] Sitaram Emani,[2,*] and L. Mahadevan[1,3,4,†]
[1]School of Engineering and Applied Sciences, Harvard University, Cambridge, Massachusetts 02138
[2]Boston Children's Hospital, Boston, Massachusetts 02115, USA
[3]Department of Physics, Harvard University, Cambridge, Massachusetts 02138
[4]Department of Organismic and Evolutionary Biology, Harvard University, Cambridge, Massachusetts 02138

(Received 9 June 2025; accepted 28 July 2026; published 5 October 2026; corrected 21 October 2026)

Biological valves control the directionality of oscillatory or fluctuating internal flows by deforming (reversibly) to stop flow. To uncover the physical basis for flow rectification in these systems, we introduce a simple physical mimic of the mitral heart valve that is shaped like a soft conical shell in an impinging flow. Combining *ex vivo* porcine-heart and *in vitro* conical valve experiments, we show how noise-activated buckling deformations serve to rectify the flow. We quantitatively explain our observations using a minimal elastohydrodynamic theory for valve closure that leads to a dynamical bifurcation driven by stochastic hydrodynamic forces. Our theory also suggests that valve collapse can be triggered on demand, which we corroborate using experiments. Together, these results suggest a design principle for the efficient operation of soft valves.

DOI: 10.1103/h78n-3582

Across the tree of life, soft elastic valves in cardiac, vascular, and lymphatic systems act as passive rectifiers, enforcing directionality in oscillatory or fluctuating flows interacting with compliant structures [1–3]. Even though the valves operate in regimes characterized by large Reynolds numbers and substantial fluctuations in flow, while also being subject to large elastic deformations, rectification emerges without active control. Classical experimental studies have established the central role of fluid-structure interaction in valvular function [4–6], while computational approaches have increasingly resolved anatomical detail and physiological loading conditions [7–13]. However, all work to date is limited to deterministic mechanisms that do not describe the onset of the dynamics of valve closure or the role of hydrodynamic fluctuations in this process.

Heart valves highlight this challenge. A mammalian mitral valve consists of soft leaflets arranged around an annulus and tethered by chordae tendineae, forming a deformable orifice that closes under adverse pressure gradients [Fig. 1(a)i]. Its operation involves large dynamic deformations that couple flow and tissue elasticity, as well as self-contact in a highly variable dynamical environment.

To understand the nature of the flow characteristics associated with valve closure, we start with a freshly harvested but nonbeating porcine heart subject to a reverse pressure gradient across its mitral valve [Fig. 1(a)ii]. Measuring the time evolution of the *orifice area,* S_m, Fig. 1(b) reveals that the mitral leaflets deform only gently under a small reverse pressure gradient (purple), but close rather suddenly when the gradient exceeds a threshold (red). In this functional state, the valve seals tightly, forming a coaptation (self-contacting) state that prevents backflow [Fig. 1(c); see Supplemental Material (SM) [14] for experimental details]. To distill the elastohydrodynamic characteristics of valve closure, we now introduce a minimal experimental setup.

Our physical mimic of the mitral valve [Fig. 1(a)] is a thin elastomeric *conical shell* fabricated using vinylpolysiloxane (Zhermack). The base and orifice radii of the cone are r_b and r_o, respectively, corresponding to a half-opening angle α [Fig. 1(d)]. The soft shell is mounted in an acrylic tube with a matching radius, through which deionized water is driven by a flow controller (Elveflow). The flow rate and pressure drop across the shell are monitored with a turbine flow meter (Vision Turbine Meters) and a differential pressure transducer (Validyne). A high-speed camera (Phantom) aligned along the cone axis registers the shape of the cone orifice subject to flow. The details of our setup, as well as the parameters of various conical shells investigated are included in SM [14].

Measuring the time evolution of the orifice area, S, from this simple physical mimic [Fig. 1(e)] reveals behaviors similar to the biological counterpart [Fig. 1(b)]: increasing the reverse flow (from purple to red) drives a sharp transition from weak orifice reduction to total collapse ($S \to 0$). In addition, both the porcine mitral valve and the conical shell exhibit a two-leaflet coaptation with a branched coaptation line at closure [cyan dashed curves, Figs. 1(c) and 1(f)]. This similarity, extending from the

*Contact author: sitaram.emani@cardio.chboston.org
†Contact author: lmahadev@g.harvard.edu

 © 2026 American Physical Society

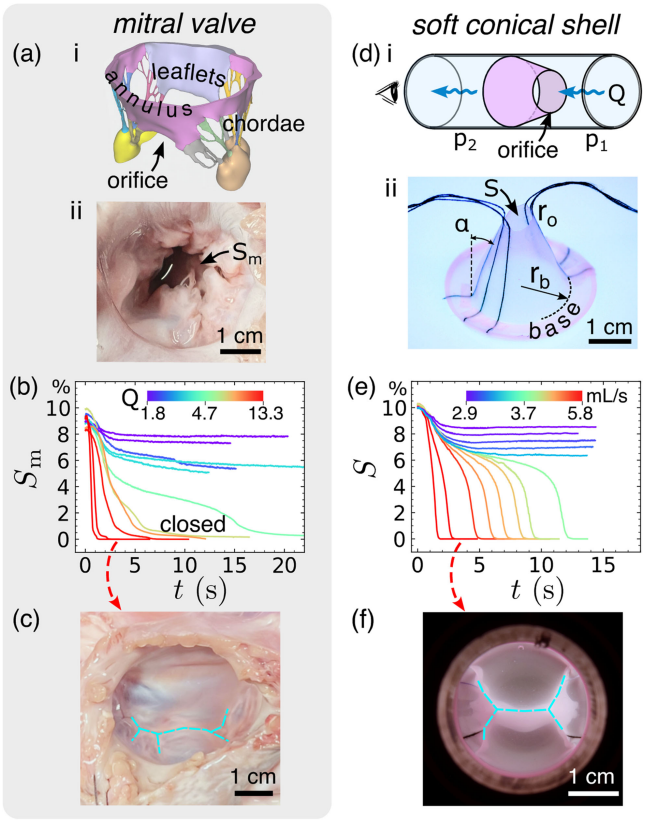


FIG. 1. A soft conical shell mimics a heart valve. (a)i Three-dimensional reconstruction of an ovine mitral valve, adapted from [10]. (a)ii Mitral valve of a Yorkshire pig heart. (d) Tethered polymeric conical shell placed under flow. (b), (e) Orifice size (normalized by the size of the annulus or cone base) as a function of time at various flow rates. (c), (f) Closed states of both valves. Cyan dashed curves: coaptation lines.

orifice evolution to the final coaptation configuration, suggests that the essential features of passive biological rectification can be captured by a much simpler geometry. In this Letter, we focus on the *initiation* of valve closure. Since the chordae system [Fig. 1(d)ii] remains slack up to coaptation, its influence on the dynamical process is negligible. Below, we focus on bare conical shells without tethering.

Figures 2(a)–2(d) display the temporal sequence of a conical shell deforming under an impinging flow that is gradually increased. Initially, a small oscillation is excited at the free edge, periodically sweeping out area δS [red and blue regions, Fig. 2(a)] [12]. As the flow rate increases, the oscillation amplitude increases, causing a lobe to buckle inward [Fig. 2(b)]. The cone then collapses into a state of coaptation, forming a seal that prevents reverse flow [Fig. 2(c)]. Further increasing the flow eventually forces the shell to evert, leading to valve failure through backward opening and subsequent reverse flow [Fig. 2(d)], analogous to the electric breakdown of a diode circuit [15].

During this process, we measure the pressure drop, $p \equiv p_1 - p_2$, and the flow rate, Q, across the cone. In the p-Q space [Fig. 3(a)], the system first follows a smooth trajectory with a steadily increasing flow $Q > 0$ (blue markers). Upon reaching a threshold, (p^*, Q^*) (black open circle), there is a discontinuous transition (blue dashed arrow), and the system abruptly switches to an *eversion branch* (cyan markers). Further increasing the flow extends this branch. We note that an axially loaded conical shell buckles at the threshold force $f_s = 4\pi\sqrt{YB}\cos^2\alpha$, where Y and B are the stretching and bending moduli [16]. This offers a pressure reference $p_s = f_s/[\pi(r_b^2 - r_o^2)] \approx 204$ Pa, in agreement with the order of magnitude of the experimentally measured $p^* \sim 10^2$ Pa [17]. In contrast, if the fluid is driven along the direction of narrowing of the cone ($Q < 0$, "forward" branch), the cone responds minimally, producing a featureless p-Q trajectory (magenta markers, III quadrant) roughly symmetric to the impinging branch.

The flow parameters at the threshold point (p^*, Q^*) give a Reynolds number $\mathrm{Re} = 2Q^*/(\pi r_o \nu) \sim 10^3$, where ν is the kinematic viscosity of water. In such situations, we expect significant fluctuations in the velocity, confirmed by flow visualization using polyamide particles (see End Matter). Given the subcritical nature of shell buckling [18,19], we expect the observed buckling transition of the cone to happen well below the ideal limit and to be driven by dynamical fluctuations in the fluid loading. To study this experimentally, we actively perturb the impinging flow using a syringe connected upstream of the cone. As a result, the p-Q trajectory under a noisy flow [red markers, Fig. 3(a)] transitions much earlier (red open star) to a distinct *coaptation branch* (red dashed arrow). The subsequent flow rate remains low for an extended pressure range. This early transition facilitates a flow *rectification*, leading to a prominent differential resistance between impinging (red) and forward (magenta) flows.

A unified picture of the parabolic p-Q curves in Fig. 3(a) follows simply from Bernoulli's equation, which yields

$$Q = \sqrt{2}CS\sqrt{\frac{p}{\rho}}, \tag{1}$$

where C is the *effective coefficient of contraction* [20], further discussed in the End Matter. Rescaling using $\bar{p} \equiv p/p_s$ and $\bar{Q} \equiv Q\sqrt{\rho/p_s}/(\sqrt{2}CS)$ collapses all p-Q branches into a single $\bar{p}$-$\bar{Q}$ [Fig. 3(b); see End Matter]. The coaptation transition under noisy flow [red open star, Fig. 3(b)] occurs at a pressure gradient an order of magnitude lower than that for the controlled steady flow (black open circle), suggesting the critical role of noise in activating the transition.

To examine this fluctuation-driven buckling process in physical space, we use high-speed imaging to measure the variation of the cross-section area of the cone orifice, $\delta S(t) \equiv \int_0^{2\pi} |r(\phi, t) - r_o| r_o \mathrm{d}\phi$ [combined area of blue and

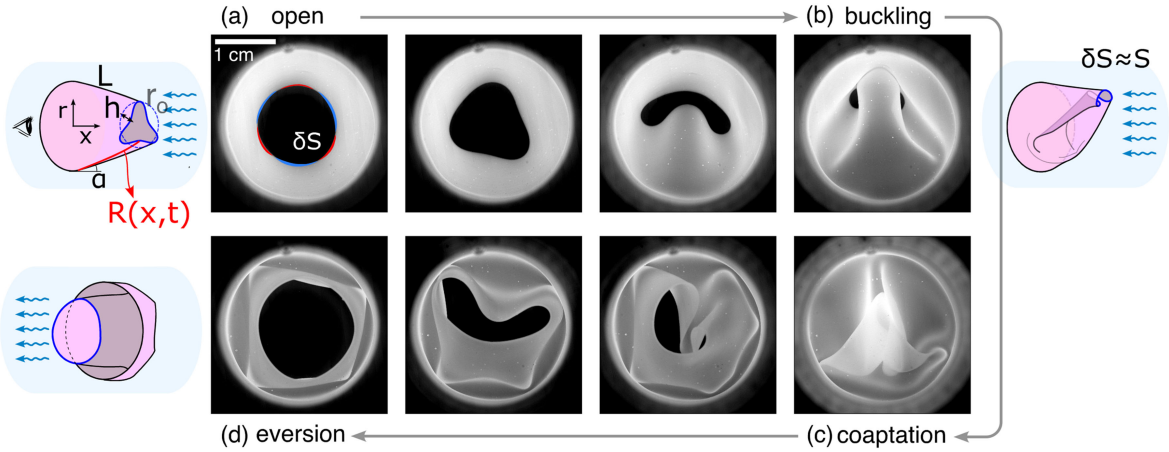


FIG. 2. High-speed images of a conical shell valve ($\alpha = 10°$) buckling and everting under an impinging flow (ramping to an adverse pressure $p \approx 100$ Pa). The shell first oscillates (a) before buckling (b) to form a coaptation state (c). The shell eventually everts (d) at high p if not tethered. The schematics show the oscillating, buckled, and everted states of the cone. Coloring superimposed in (a): the area δS formed by the inward (blue) and outward (red) deformations of the orifice edge.

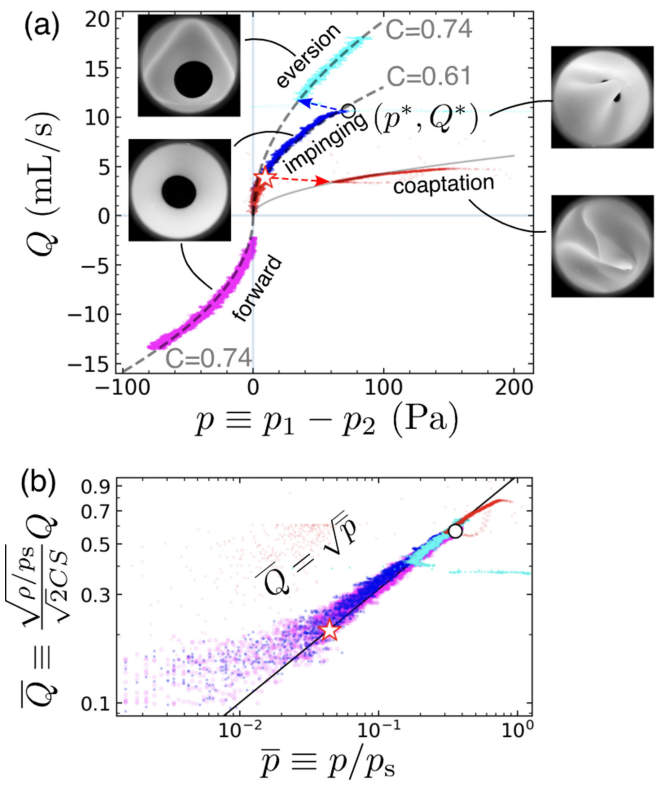


FIG. 3. The pressure-flow (p-Q) relation for a flow passing a conical shell of $\alpha = 20°$. (a) The flow rate (Q) as a function of the pressure drop (p), for the flow along (magenta) or against (blue) the direction of narrowing of the cone. At (p^*, Q^*) (black open circle), the system buckles abruptly into an everted state (cyan). Injected flow noise causes an early buckling transition (red open star), resulting in a coaptation branch (red). Photographs: corresponding orifice shape for each branch. Dashed and solid curves: predictions from Eq. (1). (b) Rescaled pressure-flow relation, $\bar{p}$-$\bar{Q}$, collapsing all branches. Solid line: $\bar{Q} = \sqrt{\bar{p}}$.

red regions in Fig. 2(a)], where $r(\phi, t)$ is the orifice edge in polar coordinates [21]. Figure 4(a) shows that under a weak impinging flow, the orifice first contracts, producing an initial excursion in the δS-t curve, followed by a fluctuating state (purple). As the flow rate Q increases, both the mean and the amplitude of the oscillation increase (blue). Near the threshold Q^*, the fluctuation amplitude can become large enough to collapse the cone probabilistically (cyan diverging curves). At $Q > Q^*$, the orifice closes deterministically without entering the fluctuating state (red).

A minimal description of the buckling onset in flow is afforded in terms of the dominant mode n [Fig. 4(a)] of the small oscillation in the cone via the relation $\delta S(t) \approx \int_0^{2\pi} |h(t) \cos n\phi| r_o d\phi = 4 r_o h(t)$, where $h(t) > 0$ is the amplitude of the standing wave around the rest shape of the orifice edge $r = r_o$ (see schematic of Fig. 2). For a cone of length L, thickness e and Young's modulus E in a fluid of density ρ, we may then write a one-dimensional elastohydrodynamic equation of motion [22,23] for $h(t)$,

$$\rho L h_{tt} + D h_t + f_{el}(h) = \Delta P. \tag{2}$$

The first term is due to the added-mass inertia of the surrounding fluid of density ρ displaced by the cone's motion [24]. Seeking a harmonic solution for h, this term scales as $\rho L h \omega^2$ with a characteristic frequency ω. The second term corresponds to a linear damping. To compare to critical damping, we can further express the coefficient $D \equiv \rho L \times 2\zeta\omega$ using the damping ratio ζ from standard oscillator theory.

The third term in Eq. (2) represents the elastic restoring stress. At small deformation h, an n-fold azimuthal bending of the orifice gives a linear stress $E e^3 n^4 h/(2\pi r_o)^4$ (see SM [14]). To capture the nonlinearity of a buckling cone, we

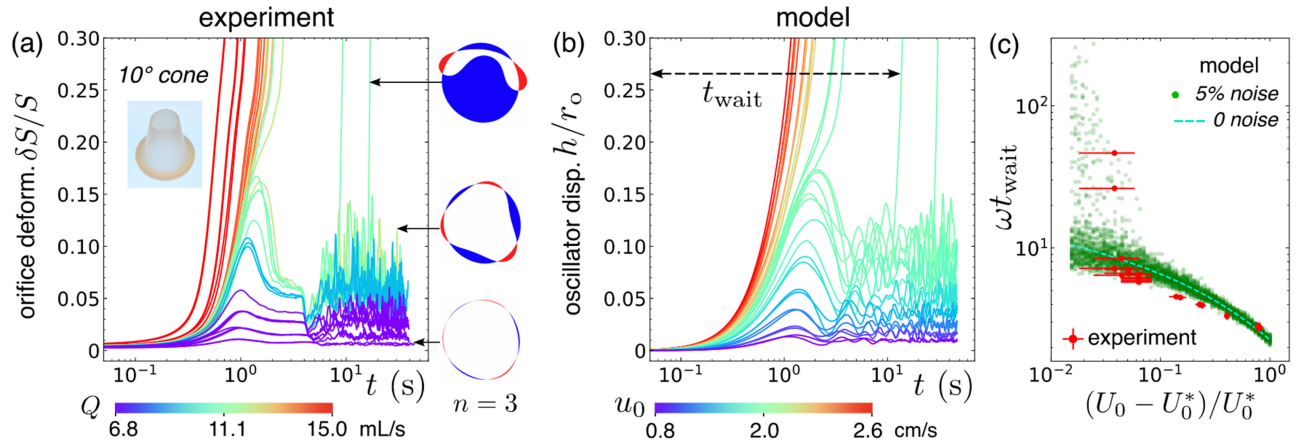


FIG. 4. Comparing experiment and theory for the flow-induced coaptation transition for a cone of $\alpha = 10°$. (a) Measured orifice deformation, $\delta S/S$, under various flow rates (color bar). (b) Time evolution of the displacement $x \equiv h/r_o$ from Eq. (3) (see SM [14] for parameter values) at various flow velocities (color bar). t_{wait}: the waiting time for the oscillator to diverge. (c) The normalized waiting time, ωt_{wait}, for the cone to buckle (red markers, $\omega = 2.66$) and for the model oscillator to diverge (green dots, 5% noise), all plotted as a function of the normalized distance to the threshold, $(U_0 - U_0^*)/U_0^*$. Cyan dashed curve: the waiting time given by the model with no flow noise.

incorporate higher-order terms through a Landau-like expansion $f_{el} \sim Ee^3n^4/(2\pi r_o)^4(h - h^2/\lambda + \ldots)$. Since a conical shape breaks $h \to -h$ symmetry, the lowest-order nonlinear term necessary is quadratic $\mathcal{O}(h^2)$, whose coefficient gives a buckling length scale λ corresponding to $f_{el}(\lambda) = 0$. Balancing the first and third terms in Eq. (2) gives the scaling of $\omega \propto \sqrt{E/\rho}n^2e^{3/2}r_o^{-2}L^{-1/2}$ [25].

Lastly, ΔP is the driving pressure across the shell wall [22,26], associated with a fluid parcel sweeping along the shell with side profile $R(x, t)$ with velocity u (see schematic of Fig. 2). Because of deflections by the shell, this parcel acquires a momentum normal to the impinging direction with a magnitude $\rho \mathrm{D}R/\mathrm{D}t$, where $\mathrm{D}/\mathrm{D}t = \partial_t + u\partial_x$ is the total derivative. The reaction stress on the shell wall from this momentum transfer is therefore $\Delta P = \rho u[\partial_t h + u(h/L + \alpha)]$ (to the lowest order). To complete the formulation, we decompose the flow velocity, $u = u_0 + u'$ into the mean flow (u_0) and a persistent fluctuation (u') [27]. We then model the mean-reverting u as the Ornstein-Uhlenbeck process $\mathrm{d}u' = -\theta u'\mathrm{d}t + \sigma\sqrt{\mathrm{d}t}Z$, where Z is the standard normal distribution. The parameters θ, σ control the autocorrelation time $\tau_\theta = 1/\theta$, and the variance $\langle u'^2\rangle = \sigma^2/(2\theta)$.

Rescaling Eq. (2) using the definitions $x \equiv h/r_o$, $\Lambda \equiv \lambda/r_o$, $\tau \equiv t\omega$, $U = U_0 + U' \equiv (u_0 + u')/(\omega L)$, and $A \equiv \alpha L/r_o$ leads to an equation for a stochastic driven-damped nonlinear oscillator,

$$\frac{\mathrm{d}^2x}{\mathrm{d}\tau^2} + (2\zeta - U)\frac{\mathrm{d}x}{\mathrm{d}\tau} - \frac{x^2}{\Lambda} + (1 - U^2)x - AU^2 = 0. \quad (3)$$

Without noise, this reduces to the normal form for an inertial version of a saddle-node bifurcation [28] with two equilibria $x_\pm = (\Lambda/2)[1 - U_0^2 \pm \sqrt{(1 - U_0^2)^2 - 4U_0^2A/\Lambda}]$, one stable and the other unstable, that coalesce as U_0 increases past the bifurcation point U_{bi}. The threshold velocity, $U_0^*(\zeta, \Lambda, A) \equiv u_0^*/(\omega L)$, defines the *separatrix* between converging and diverging trajectories in phase space (see SM [14] for a detailed analysis).

Incorporating noise and estimating the parameters in Eq. (3) (SM [14]), we integrate Eq. (3) with a time step of $\Delta\tau/\omega \ll 1/\theta$ [29], which yields the results shown in Fig. 4(b). In the marginal case where $U_0 \to U_0^*$, the oscillator fluctuates with a large amplitude and can diverge, but only by chance (cyan). By comparing Figs. 4(a) and 4(b), we see that our low-dimensional model captures the basic physics of the instability as a subcritical bifurcation with a threshold, producing results that are qualitatively similar to the trends seen in our experiments. While our model does not capture the fine structure within the initial excursion in the data [a peak followed by a plateau, $t = 1 \sim 4$ s, in Fig. 4(a)] due to our omission of the complex coupling of the eddying flow with the dynamics of shell buckling, it does allow us to probe the effects of noise quantitatively.

In particular, we can track the waiting time t_{wait} for the oscillator response to diverge [indicated in Fig. 4(b)] as a function of the mean velocity U_0. In Fig. 4(c), we show the deterministic limit of a laminar flow $U' = 0$ ("0 noise," cyan dashed curve). With a noise of the scaled amplitude $\sqrt{\langle U'^2\rangle}/U_0 = 0.05$, there is a spread in the waiting time t_{wait} ("5% noise," green dots); the scatter widens to give an exponential tail as $U_0 \to U_0^*$ (see SM [14]), suggesting a Kramers process with a rare, memoryless escape from the metastable well around the focus x_-. For comparison with this minimal theory, we plot the experimentally measured buckling times for the corresponding cone (red), and find good agreement in the broadening of t_{wait}. In SM [14], we

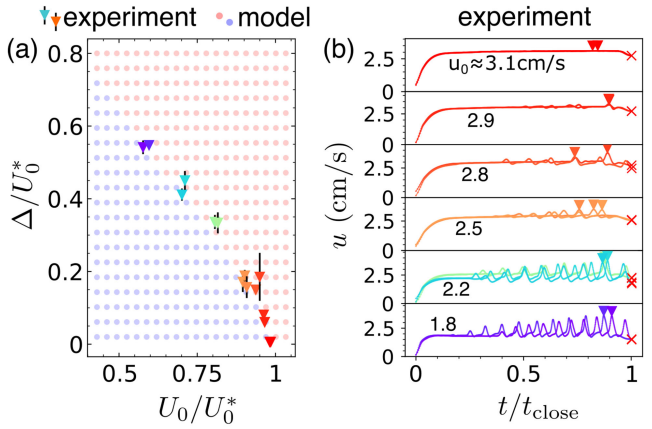


FIG. 5. Controlling closure with disturbances. (a) The disturbance amplitude Δ required to trigger a transition ($\alpha = 20°$) as a function of base flow U_0, both normalized by the threshold velocity at zero disturbanceU_0^*. Blue (red) dots: converging (diverging) solutions given by Eq. (3) at $\tau \to \infty$. (b) Experimental sequences of noise spikes of increasing amplitudes are injected to various base flows (u_0) until the cone collapses (red crosses) at t_{close}. Multiple trials are shown for each base velocity, u_0. Triangular markers in (a) and (b): measured minimal disturbance required to collapse the cone at various impinging flows.

show that the same framework consistently captures the transition of a cone with a different geometry, $\alpha = 20°$.

With our ability to understand the stochastic dynamics of valve closure, we ask whether we can *trigger* the coaptation transition on demand by tuning the amplitude of the flow fluctuations. This is functionally relevant as it provides a natural way to control the rectification transition for the valve in both artificial and natural settings. To do so in the context of Eq. (3), we consider an incoming flow of $U = U_0 + \delta U$ where $\delta U = \Delta e^{-\tau^2/2\Sigma^2}$ is an isolated disturbance with a prescribed amplitude (setting the disturbance duration $\Sigma/\omega = 0.5$ s). The impulsive form of the disturbance serves to facilitate experimental verification via an easily generated spike, while providing an analog for pulsatile flow disturbances common in biological conditions, e.g., the pumping motion of the heart. To determine the disturbance amplitude required for the collapse, we scan the space of the mean and fluctuating velocities (U_0-Δ, normalized) by solving Eq. (3) for the long-time end states ($\tau \to \infty$). Figure 5(a) shows a well-defined boundary between diverging (red dots) and stationary (blue dots) solutions. Experimentally, we use the syringe connected to the setup to inject a sequence of spikes (duration 0.5 s) of progressively increasing amplitude until the cone collapses [Fig. 5(b)]. Plotted in the $U_0 - \Delta$ plane, the measured minimal collapse-inducing spikes [triangles, with marker styles consistent between Figs. 5(a) and 5(b)] cluster tightly around the simulated phase boundary in Fig. 5(a). This provides strong evidence for the efficacy of our minimal model in predicting different valve states in a functional setting.

Inspired by the geometry and dynamics of mitral valve function as a soft flow-driven rectifier, we created a simple physical mimic using a thin elastic conical valve that can undergo a flow-driven subcritical bifurcation and buckle into a functional state that prevents backflow. A minimal stochastic theory allows us to explain our observations and quantitatively predict this transition and the waiting time for the onset of closure as a function of the noise amplitude. Further experiments demonstrate that the rectification transition can be triggered on demand by controlled disturbances, thus naturally providing a means to guide it dynamically, and showing how fluctuations *enhance* the rectification transition in soft valves.

Coming back full circle, our work suggests that the contractions of myocardium or papillary muscles in the heart might provide impulsive spikes and likely guide the passive interactions to trigger valve closure. Addressing this quantitatively naturally leads to questions for future study that include introducing periodic flow forcing, accounting for restraining forces from the tethering chordae, and integrating the softness of the surrounding walls of lymphatic vessels [13], veins, or hearts.

Acknowledgments—We thank the Simons Foundation, the Henri Seydoux Fund, the TreeFrog Fund, and Boston Children's Hospital for partial financial support.

Data availability—The data that support the findings of this article are openly available [31].

[1] C. S. Peskin, The fluid dynamics of heart valves: Experimental, theoretical, and computational methods, Annu. Rev. Fluid Mech. **14**, 235 (1982).
[2] J. B. Grotberg and O. E. Jensen, Biofluid mechanics in flexible tubes, Annu. Rev. Fluid Mech. **36**, 121 (2004).
[3] M. Heil and A. L. Hazel, Fluid-structure interaction in internal physiological flows, Annu. Rev. Fluid Mech. **43**, 141 (2011).
[4] B. J. Bellhouse and F. H. Bellhouse, Mechanism of closure of the aortic valve, Nature (London) **217**, 86 (1968).
[5] C. S. F. Lee and L. Talbot, A fluid-mechanical study of the closure of heart valves, J. Fluid Mech. **91**, 41 (1979).
[6] E. L. Yellin, C. Peskin, C. Yoran, M. Koenigsberg, M. Matsumoto, S. Laniado, D. McQueen, D. Shore, and R. W. Frater, Mechanisms of mitral valve motion during diastole, Am. J. Physiol. **241**, H389 (1981).
[7] C. S. Peskin, Flow patterns around heart valves: A numerical method, J. Comput. Phys. **10**, 252 (1972).
[8] D. M. McQueen, C. S. Peskin, and E. L. Yellin, Fluid dynamics of the mitral valve: Physiological aspects of a mathematical model, Am. J. Physiol. **242**, H1095 (1982).
[9] F. Sotiropoulos, T. B. Le, and A. Gilmanov, Fluid mechanics of heart valves and their replacements, Annu. Rev. Fluid Mech. **48**, 259 (2016).
[10] M. Toma, M. Ø. Jensen, D. R. Einstein, A. P. Yoganathan, R. P. Cochran, and K. S. Kunzelman, Fluid–structure interaction analysis of papillary muscle forces using a

comprehensive mitral valve model with 3d chordal structure, Ann. Biomed. Eng. **44**, 942 (2016).
[11] A. D. Kaiser, D. M. McQueen, and C. S. Peskin, Modeling the mitral valve, Int. J. Num. Methods Biomed. Eng. **35**, e3240 (2019).
[12] J. H. Lee, L. N. Scotten, R. Hunt, T. G. Caranasos, J. P. Vavalle, and B. E. Griffith, Bioprosthetic aortic valve diameter and thickness are directly related to leaflet fluttering: Results from a combined experimental and computational modeling study, JTCVS Open **6**, 60 (2021).
[13] B. Kaoui, A. Bou Orm, P. Navet, J. Baish, and L. L. Munn, Bicuspid valve closure and backflow prevention: Role of leaflet geometry, Phys. Rev. Fluids **11**, 033103 (2026).
[14] See Supplemental Material at http://link.aps.org/supplemental/10.1103/h78n-3582 for experimental methods and details of the stochastic oscillator model.
[15] S. Sze, Y. Li, and K. Ng, *Physics of Semiconductor Devices* (Wiley, New York), p. 102.
[16] P. Seide, Axisymmetrical buckling of circular cones under axial compression, J. Appl. Mech. **23**, 625 (1956).
[17] However, we note that our loading is not strictly axial so this merely serves as an order of magnitude comparison.
[18] W. Koiter, The effect of axisymmetric imperfections on the buckling of cylindrical shells under axial compression, Mechanics 265 (1963).
[19] J. M. T. Thompson, Advances in shell buckling: Theory and experiments, Int. J. Bifurcation Chaos Appl. Sci. Eng. **25**, 1530001 (2015).
[20] E. Zarantanello and G. Birkhoff, *Jets, Wakes, and Cavities*, Applied mathematics and mechanics (Academic Press, New York, 2012) Chap. 1.
[21] We have verified that a few other definitions of the orifice deformation give essentially the same result, while the area measure adopted here has the advantage of robustness and ease of computation.
[22] M. Argentina and L. Mahadevan, Fluid-flow-induced flutter of a flag, Proc. Natl. Acad. Sci. U.S.A. **102**, 1829 (2005).
[23] S. Mandre and L. Mahadevan, A generalized theory of viscous and inviscid flutter, Proc. R. Soc. A **466**, 141 (2010).
[24] We neglected the mass of the shell relative to that of the fluid displaced since $\rho_{\text{shell}} \approx \rho$ but $e \approx 10^{-2}L$ so that $\rho_{\text{shell}} e \ll \rho L$.
[25] E. Virot, V. Spandan, L. Niu, W. M. van Rees, and L. Mahadevan, Elastohydrodynamic scaling law for heart rates, Phys. Rev. Lett. **125**, 058102 (2020).
[26] M. J. Lighthill, Hydromechanics of aquatic animal propulsion, Annu. Rev. Fluid Mech. **1**, 413 (1969).
[27] S. B. Pope, *Turbulent Flows* (Cambridge University Press, Cambridge, England, 2000).
[28] C. Kuehn *et al.*, *Multiple Time Scale Dynamics* (Springer, New York, 2015), Vol. 191, p. 62.
[29] Under this condition, Itô and Stratonovich interpretations converge. We use a Runge-Kutta scheme for numerical integration. See Supplemental Material and the included Ref. [30].
[30] N. G. van Kampen, Itô versus Stratonovich, J. Stat. Phys. **24**, 175 (1981).
[31] M. He, S. Cho, G. Dafflisio, S. Emani, and L. Mahadevan, Stochastic elastohydrodynamics of soft valves, Zenodo, 2026, http://doi.org/10.5281/zenodo.21699256.

Correction: Reference [31] has been rectified to provide the correct source information for the data.

End Matter

Pressure-flow (p-Q) relation—In this section, we unpack details of the physical picture giving rise to the p-Q relation shown in Fig. 3. We track the local pressure drop across the cone, $p \equiv p_1 - p_2$, and the flow rate, Q, simultaneously as a function of time, t. As the far-field driving pressure is gradually ramped up, both p and Q increase steadily with t. Once the threshold (p^*, Q^*) is reached, the cone buckles and everts, causing p to drop after a sharp spike [Fig. 6(a)]. Synchronizing the time series of $p(t)$ and $Q(t)$ gives the p-Q trajectory in Fig. 3(a). If we actively introduce perturbations with a syringe connected in front of the cone, the cone collapses at a much smaller p^* and Q^* [Fig. 6(b)], making the p-Q trajectory reach an earlier threshold (p^*, Q^*) (red open star, Fig. 3) to transition to a coaptation state. Further increasing the reverse pressure everts the cone [beyond p_{break} in Fig. 6(b)], turning it inside out and open to the back.

We visualize the flow around the conical valve using polyamide seeding particles (50 μm, Dantec Dynamics). The particle streaks in Fig. 7, shown for two opposite flow directions, reveal that the flow contracts into a narrower downstream jet whether it moves with or against the cone's narrowing direction, owing to fluid inertia as it passes the cone lip. This supports the flow configurations sketched beside each photograph in the right panel of Fig. 7. We

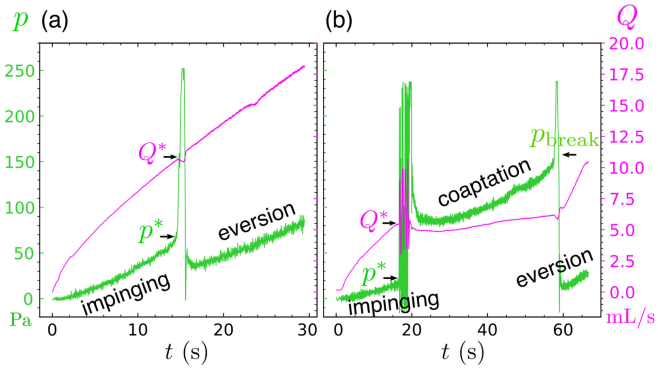


FIG. 6. Time sequence of the pressure p-t (green) and the flow rate Q-t (magenta) for (a) a steadily increasing flow past a conical shell, and (b) a flow with a short noise burst at ≈18 s, collapsing it at much smaller p^* and Q^*.

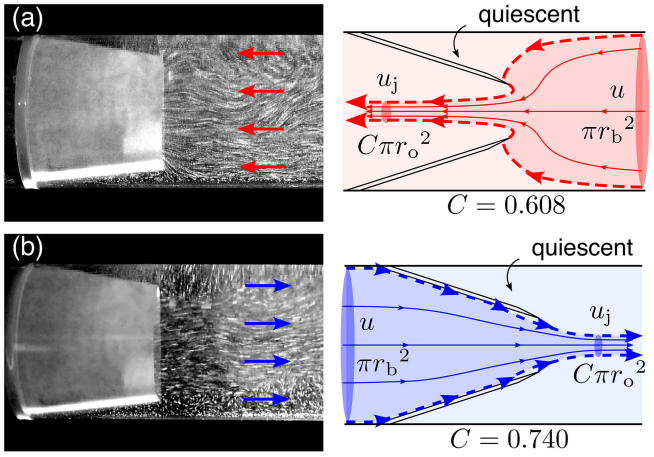


FIG. 7. The velocity field visualized by seeding particles for a flow against or along the direction of narrowing of a conical shell. Schematics: corresponding flow configurations giving rise to Eq. (A1). Dashed lines: velocity discontinuities (Helmholtz vortex sheets) that separate the jet (dark) and the quiescent regions (light).

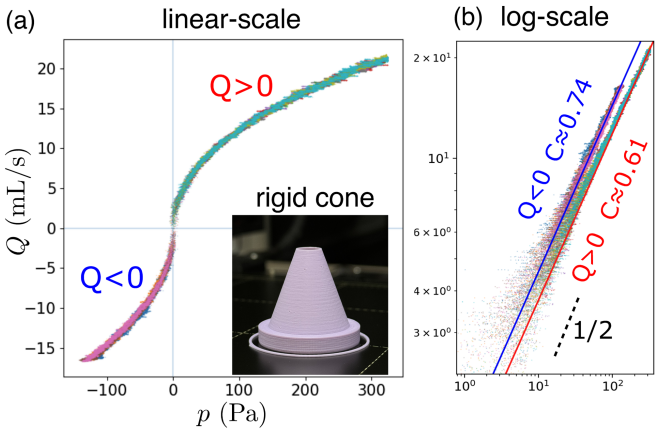


FIG. 8. (a) Pressure flow (p-Q) relation measured from a rigid cone of half-opening angle $\alpha = 20°$ (photograph). (b) Logarithmic scale of the same data as in (a). The effective coefficient C (0.74 or 0.61 for two flow directions) is extracted. Markers of different colors represent repeated experiments.

therefore model the flow as an axisymmetric free-surface flow, with the jet (dark shade) separated from the quiescent regions (light shade) by velocity discontinuities, i.e., Helmholtz vortex sheets (thick dashed lines).

The Reynolds number of $\mathrm{Re} \sim 10^3$ justifies the idealization of an inviscid flow. In the flow configuration of either Fig. 7(a) or 7(b), the flow (of density ρ) passes through two circular cross sections of areas πr_b^2, $\pi r_o^2 C$ with velocities u, u_j, respectively. Here, C is the *coefficient of contraction* that describes the reduction of the cross-section area of a jet emanating from an orifice [20], which depends on the flow direction. Bernoulli's principle and the conservation of flux lead to $p/\rho = (u_j^2 - u^2)/2$ and $u\pi r_b^2 = u_j \pi r_o^2 C$. Eliminating u_j, the flow rate across the junction is

$$Q \equiv u\pi r_b^2 = \frac{C\pi r_o^2 r_b^2}{\sqrt{r_b^4 - C^2 r_o^4}} \sqrt{\frac{2p}{\rho}} \approx CS\sqrt{\frac{2p}{\rho}}. \qquad \text{(A1)}$$

In the last step, we have used the definition $S \equiv \pi r_o^2$ for an undeformed cone, and the approximation $r_o^4 \ll r_b^4$, a lenient simplification that holds for all cones used in our experiments (see SM [14]).

Equation (A1) has been formally derived for a *laminar* flow through a conical shell. To take into account flow fluctuations at $\mathrm{Re} \sim 10^3$ in our experiments, we maintain the intuitive laminar description giving rise to Eq. (A1), but absorb all fluctuating effects into the coefficient C. To obtain this effective value of C, we measure the p-Q relation in a *rigid* conical shell (3D printed polylactic acid) matching the geometry of the soft cone used in Fig. 3. Figure 8(a) shows that through repeated experiments (different colors), the p-Q curves for the fluctuating flow around a rigid cone cluster well into two distinct branches of square-root relations for two directions, supporting our assumption that the complex effects of fluctuation can be captured by a single effective C for each case. From the logarithmic scale in Fig. 8(b), we extract that $C = 0.61$ for $Q > 0$, while $C = 0.74$ for $Q < 0$. These values measured from a rigid cone are in good agreement with the corresponding measurements from a *soft* cone up until its collapse in Fig. 3 (red open star or black open circle).

Even when the cone has everted, the p-Q curve still follows a square-root relation (cyan markers, Fig. 3). In this state, the flow is along the pointing direction of the everted cone. Therefore, we use $C = 0.74$ in Eq. (A1) for this state. Interestingly, the orifice size S for the everted state is measured to be slightly larger than that of the normal state. Substituting the area of this everted orifice into Eq. (A1) gives excellent agreement with our measured data [top dashed curve, I quadrant, Fig. 3(a)]. The sharp jump in the p-Q trend is therefore fully explained by two factors as the cone everts: (i) C increases from 0.61 to 0.74, and (ii) S becomes slightly enlarged [compare the two photographs corresponding to the impinging and eversion branches in Fig. 3(a)].

In the presence of strong external noise, the cone collapses early. Instead of entering the state of eversion, the cone is *crumpled* by the weaker flow to a state of coaptation, where small leaking channels form, allowing a small flow [coaptation branch, Fig. 3(a)]. Although the orifice of the coaptation state cannot be seen, the p-Q relation can still be fitted by a square-root curve when we use the combination of CS as a fitting parameter [solid curve, I quadrant, Fig. 3(a)]. Taken together, these considerations collapse the multiple branches in Fig. 3(a) onto the single curve shown in Fig. 3(b).